

## NAVT-net neuron attention visual taylor network for lung cancer detection using CT images

Lokanathan Jimson <sup>a,\*</sup>, John Patrick Ananth <sup>b</sup>

<sup>a</sup> Department of Artificial Intelligence and Machine Learning, DMI College of Engineering, Palanchur, Chennai - 602103, India

<sup>b</sup> Department of Computer Science and Engineering, Sri Krishna College of Engineering and Technology, Coimbatore - 641008, India



### ARTICLE INFO

#### Keywords:

Lung Cancer detection  
Computed Tomography images  
Homomorphic filtering  
Dual-branch-UNet  
Neuron Attention Visual Taylor Network

### ABSTRACT

Lung Cancer is regarded as a common fatal disease affecting humans throughout the entire world. Early diagnosis is vital to save the patient's life and Computed Tomography (CT) scans are referred to as the major imaging modes but, the manual examination of a CT scan is time-consuming and results in errors. Hence, a novel system of Neuron Attention Visual Taylor Network (NAVT-Net) is developed to detect lung cancer. At first, the CT image is acquired, and then, the input image is filtered based on homomorphic filtering. Then, the lung nodule is segmented using the Dual-Branch-UNet (DB-UNet). Later, the image augmentation is achieved by resizing, flipping, as well as rotation. Next, the shape-based features are extracted and subjected to the last stage of lung cancer detection, which is done by the NAVT-Net system that is established on the basis of Neuron Attention Stage-by-Stage Network (NASNet), Visual Geometry Group-16 (VGG16), and Taylor series. Hence, the experimental results of the developed NAVT-Net system achieved high values of 92.176 % accuracy, 93.997 % of True Positive Rate (TPR), 92.189 % of True Negative Rate (TNR), F1-score of 90.999 %, and precision of 91.998 %, computational time, and memory usage of 37.879 s, and 41.100MB at K-values of 9.

### 1. Introduction

Generally, the Lungs are filled with air inside the thoracic cavity and are the major organ of the breathing system. The cells in the lung undergo cancerous variation (malignancy), which leads to lung cancer and is the foremost cause of death related to cancer (Siegel et al., 2022). The unregulated growth of tissue and mutation discusses the incidence of permanent variations in the sequences of Deoxyribonucleic Acid (DNA). Mutations can indeed arise due to various factors, which are commonly categorized into two, such as inherited genetic abnormalities and external factors. Usually, injured tissue is exchanged with another tissue but in the occurrence of a malicious mutation, the original growth of tissue is unregulated which is said to be malignant cells. Lung nodules are irregular tissue developments present inside the lung, which are benign or malicious. Most of the tissues are benign, but few are the signs of suspicious nodules. Recent research evaluates that only 19 % of lung cancer people can survive up to 5 years (Shafi et al., 2022). Lung cancer is regarded as the foremost cause of death worldwide, which is widely classified as small and non-small (Siegel et al., 2022). Lung cancer is a major contributor to death related to cancer globally and has the highest rate of mortality among every kind of cancer (Saha et al., 2024). The

existence chances of people with Lung cancer are distinctly better through initial diagnosis. Benign nodules are regarded as noncancerous, which won't spread to other body parts. In accordance with the World Health Organization (WHO), the rate of cancer deaths is predicted to increase to 45 % by 2030 (Shafi et al., 2022). The death rate of lung cancer is high among all types of cancer. The most dangerous disease that causes death is lung cancer, moreover, this disease is more challenging to treat at the initial stage and its symptoms can be detected at its final stage. Furthermore, the possibility and survival rate of humans can be minimized due to the early treatment and identification of cancer. In order to detect lung cancer, CT scans are regarded as the most reliable tool, as they disclose all the unsuspected and suspected nodules in the lungs. Nevertheless, anatomical structure misjudgment by radiologists and variations of intensity in CT images make the detection process more difficult (Suzuki et al., 2006). In recent days, Computer Aided Diagnosis (CAD) has been employed for assisting doctors and radiologists in identifying the cancerous cells precisely (Xiuhua et al., 2011). Further, several approaches have been introduced by researchers for detecting cancer, and they have enhanced the effectiveness and tend to detect cancer with a higher accuracy rate. In addition to this, image-processing methods are also executed for detecting and

\* Corresponding author.

E-mail address: [jimson@dmice.ac.in](mailto:jimson@dmice.ac.in) (L. Jimson).

classifying lung cancer (Makaju et al., 2018).

In addition, lung cancer is considered the second position among all kinds of cancer while considering several cases (Saha et al., 2024). This disease is regarded as a very widespread disease, which leads to cancerous deaths (Adelsmayr et al., 2023a). CT is the most important mode of image for measuring the progress/crumbling and making the decision of malignant growth of lungs. Doctors recommend many productive treatments for an outcome of the intelligent presentation of lung malignancy by CT (Dewes et al., 2016). The diagnostic approaches are biopsies, MRI scans (Magnetic Resonance Imaging), CT scans, chest radiography (X-ray), etc. But, the early-stage detection of lung cancer is difficult (Ahmed et al., 2020) (Elnakib et al., 2020). A CT scan (Shakeel et al., 2019) is referred to as a 3-D image of the body parts, which is produced by an X-ray machine that takes numerous images of similar anatomical locations from diverse angles. Besides, the conditions of intrathoracic pathology are estimated through the CT scan (Adelsmayr et al., 2023b). Typically, the specialists perform a CT scan to detect lung cancer by injecting the contrast-enhancing standard into the blood (Venkatesh and Ramana, 2022). Such a type of CT scan delivers the complete chest images of the patients to permit better lung cancer detection (Alzubaidi et al., 2021) (Asuntha and Srinivasan, 2020). This advance is highly substantial for analyzing lung cancer with the potential for wider medical integration. Deep Learning (DL) and Machine Learning (ML) are the subdivisions of Artificial Intelligence (AI), which speeds up lung cancer identification and permits scholars to observe several patients in less time. Even though a few algorithms based on Convolutional Neural Network (CNN) have offered the performances of cutting-edge but the system faces some problems for applications related to the segmentation of medical images (Crasta et al., 2024).

DL is a tool for the classification of cancer nodules by minimizing the required number of scans to attain the analysis of benign or malignant. DL approaches demonstrate promising outcomes in both benign and malignant detection (Heuvelmans et al., 2021). The systems of CAD utilize the DL models for classifying lung nodules. Besides, these systems are also employed to classify the nodule type if it is benign or suspicious (Shafi et al., 2022). The speed and precision of diagnosis are increased potentially by applying the DL schemes, but numerous obstacles are addressed while using these methods. Providing accurate segmentation, appropriate annotations, and high-quality assurance for data collection is tough. The image complexity with numerous sizes makes things more challenging since image annotation is monotonous and time-consuming, particularly for manifold image slices. Hence, a vital need is to standardize the data, which is selected precisely by skilled specialists. The skilled knowledge and substantial time are desirable to annotate the medical images to identify lung cancer (Dodia et al., 2022). The labeled data is essential to confirm the formation along with the valuation of DL systems, resulting in less-than-supreme performance. DL annotates the data automatically by using large annotation databases. An analysis of the improved model is achieved by designing the CAD systems from both medical images and clinical records (Crasta et al., 2024).

This article develops a DL system named NAVT-Net for lung cancer detection with CT images. The input CT image is subjected to the pre-processing phase to eradicate the unwanted noise using homomorphic filtering and then, the pre-processed image is passed to the segmentation stage in which the region of the lung nodule is segmented and subjected to the augmentation stage. Subsequently, the augmented image is forwarded to excerpt the shape-based features in the feature extraction stage. Consequently, the mined features are finally fed to the detection stage to detect lung cancer using NAVT-Net, which is the amalgamation of NASNet, VGG-16, as well as Taylor Series.

The foremost research contribution is,

- **Designed NAVT-Net technique for lung cancer detection:** The NAVT-Net is introduced for lung cancer detection from CT images. NAVT-Net is formed by fusing the NASNet, VGG-16, and Taylor Series.

The subsequent sections of the research are ensuing as: Section 2 analyses the former approaches for detecting lung cancer. The NAVT-Net method is elaborated in Section 3, which employs the model of NASNet and VGG16. The outcomes of the experimental analysis are deliberated in Section 4. The potential future directions and conclusion are explicated in Section 5.

## 2. Motivation

It is crucial to detect lung cancer at an early stage for minimizing the rate of mortality and to provide the proper treatment for the concerned person. The existing approaches for lung cancer detection include several techniques, but the rate of accuracy is not improved and includes only a limited amount of data with high complexity. These challenges are overcome by the developed NAVT-Net system to detect lung cancer. The pros and cons of the existing systems are embodied below.

### 2.1. Literature analysis

The prevailing schemes for detecting lung cancer are analyzed along with its positives and negatives are portrayed below.

Rehan Raza, et al., developed the scheme of EfficientNetB1-based Lung-EffNet in (Raza et al., 2023) for classifying lung cancer. The EfficientNetB1-based Lung-EffNet was quicker and required only a few parameters for training but failed to focus on the potential of Transfer Learning (TL), and had only a limited amount of data, so the accurate classification of lung cancer is difficult. The 3D lung cancer analysis system was introduced by Yahia Said, et al., in (Said et al., 2023) for segmenting the medical images, which minimized the over-fitting problems and improved the scalability. But the 3D lung cancer analysis scheme required a high-performance Graphic Processing Unit (GPU) to perform smoothly and the technique was computationally intensive. Surya Majumder, et al., presented the Mitscherlich function-based Ensemble Network (MENet) in (Majumder et al., 2024) for lung cancer classification. This MENet system was more reliable and the False Positive Rate (FPR) was low. However, MENet failed to decrease the errors. Utilized the VER-Net approach in Saha et al. (2024) for lung cancer detection, which had good generalization and exhibited high accuracy. However, VER-Net failed to attain low computational complexity.

Imran Shafi, et al., developed a DL-enabled Support Vector Machine (SVM) in Shafi et al. (2022) for diagnosing lung cancer, which took only a little time for implementation but had a high chance of over-fitting problems. In Crasta et al. (2024), established the 3D-ResNet framework for detecting and diagnosing lung cancer, which enhanced the robustness and reduced the FPR. However, this 3D-ResNet failed to train the varied databases and was not utilized in clinical trials to improve the system clarity. In Venkatesh and Ramana, (2022), employed CNN to detect lung cancer, which had the ability to handle larger databases but required the large size of network. Shalini Wankhade and Vigneshwari S introduced Cancer Cell Detection using a Hybrid Neural Network (CCDC-HNN) in Wankhade and Vigneshwari, (2023) for early lung cancer detection. This CCDC-HNN method attained high accuracy with minimum errors but failed to improve the system with the usage of cascaded classifiers.

### 2.2. Challenges

The limitations faced by the prior approaches for the detection of lung cancer are embodied as,

- The EfficientNetB1-based Lung-EffNet model introduced in Raza et al. (2023) was quick and required only a few parameters to train the model and diagnose lung cancer automatically. But failed to consider the hybrid system for improving the efficiency and accuracy of the Neural Networks to detect lung cancer at an early stage.

- The 3D lung cancer analysis system was established in Said et al. (2023), which improved the results of both the segmentation and classification and was efficient in assisting doctors as well as radiologists. However, this scheme failed to describe the lung nodule morphology and the stages of lung cancer.
- The MENet model developed in Majumder et al. (2024) attained high accuracy in lung cancer prediction but it failed to consider the augmentation to alleviate the problems of overfitting.
- VER-Net system utilized in Saha et al. (2024) achieved better accuracy and performance in lung cancer detection. However, this system failed to consider the nodule segmentation for enhancing the feature extraction and planning the better treatment.
- Traditional techniques suffer due to inadequate annotated databases, substantial intra-class variations, and inter-class similarities. Furthermore, it was an undependable and time-consuming process. In addition, class imbalance and insufficient data are considered as the main aspects that may result in overfitting.

### 3. Proposed NAVT-Net for lung cancer detection

A Novel NAVT-Net is presented for detecting lung cancer, which is important to detect lung cancer at the earlier stage of the disease to raise the survival rate of the person. Fig. 1 exemplifies the prospective outline of the NAVT-Net for detecting lung cancer with CT image, which consists of five phases, such as preprocessing, segmentation of lung nodule region, augmentation, feature extraction, as well as detection stage. The input CT image is acquired from the database (Classification, 2024) and preprocessed based on homomorphic filtering (Han et al., 2021) in the preprocessing stage. Then, the preprocessed image is passed to the lung

nodule region segmentation stage, which is used to identify the accurate region of the lung nodule using the DB-UNet (Jian et al., 2023). Later, the segmented region is fed to the image augmentation (Khosla and Saini, 2020), which is used to expand the size and helps to generalize better by minimizing the overfitting issues through the process of resizing, flipping, and rotating. Next, the feature extraction is done regarding the shape-based features (Pawar et al., 2023), where, features like nodule perimeter, area, irregularity index, and nodule solidity are extracted. Finally, lung cancer is detected by NAVT-Net, which is developed by the fusion of NASNet (Cano et al., 2021), VGG-16 (Nguyen et al., 2022), and the Taylor series (Mangai et al., 2014).

#### 3.1. Inputting CT lung image

The collection of images from the database (Classification, 2024) is the fundamental step to detect the lung cancer, and the database  $L$  including the number of images  $\gamma$  is defined as,

$$L = \{L_1, L_2, \dots, L_i, \dots, L_\gamma\} \quad (1)$$

where,  $i^{\text{th}}$  the input image for lung cancer detection is symbolized as  $L_i$  and forwarded to the following phase.

#### 3.2. Preprocessing CT image using homomorphic filtering

The input assigned to the preprocessing phase the CT image  $L_i$ , and the homomorphic filtering is used to eradicate the unwanted noise in the image and also to enhance the image quality in an efficient manner (Han et al., 2021). This filter enhances the quality of an image by lessening illumination variations, and by improving the contrast, which makes the

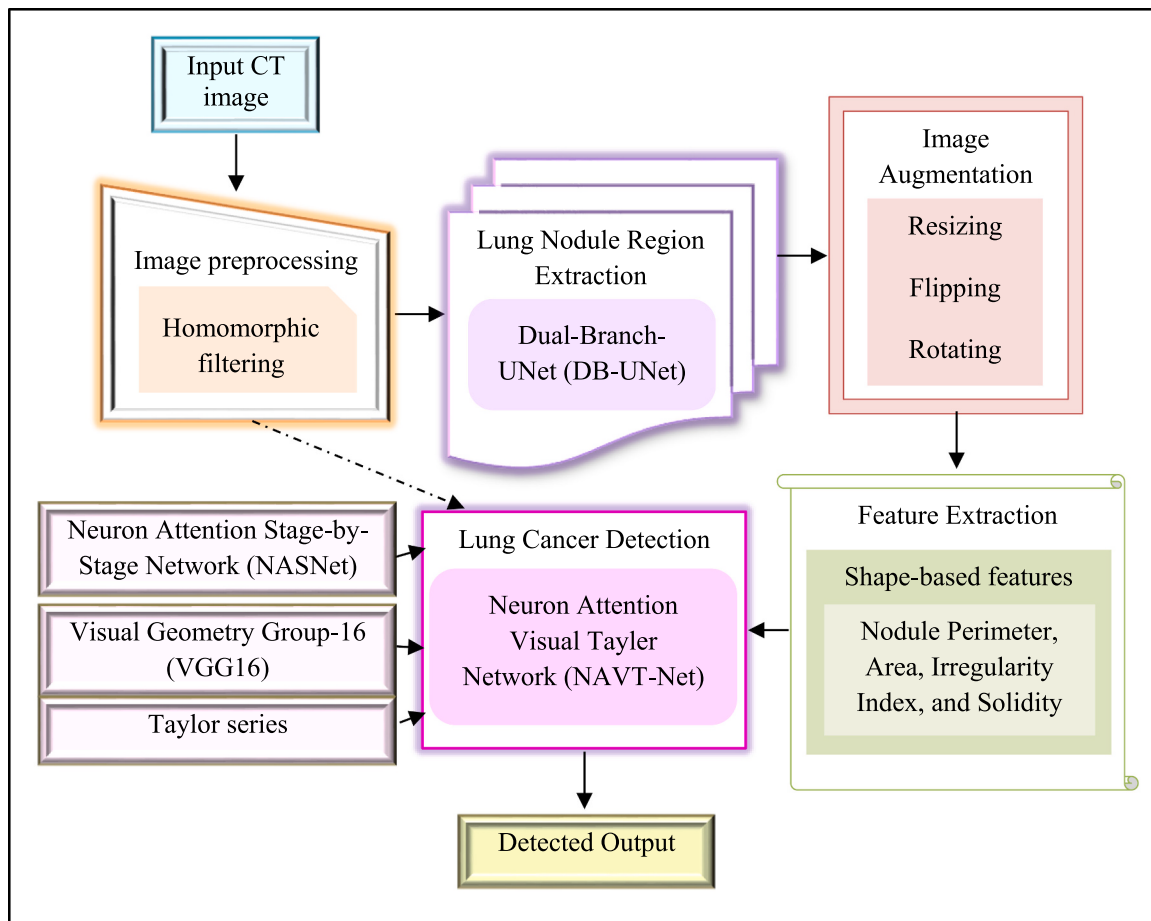


**Fig. 1.** Systematic depiction of NAVT-Net for lung cancer detection.

beneficially useful in various tasks, namely detail extraction, noise reduction, and image enhancement. Further, this process is performed by labeling the multiplicative nature of the reflectance and illumination components in the image. Here, the high-frequency component is emphasized by separating the reflectance and illumination, and it carries the textures and details of an image. Hence, the sharper edges, and finest details in the image are improved, further this filtering process minimizes the noise by improving the reflectance features. The homomorphic approach is utilized to progress the brightness of the images by handling the illumination and reflectance components separately. The image is separated into the incident element and reflection element, and the incident element finds the dynamic series of the entire image that belongs to part of low-frequency, whereas the reflection element reflects the information regarding the edge of the image that belongs to the part of high-frequency. The image and noise are combined through multiplication in the image-gathering process as expressed below,

$$g(a, b) = L_i * (c(a, b).f(a, b)) \quad (2)$$

where,  $g(a, b)$  denotes the generated image,  $c(a, b)$  indicates the incident element, and  $f(a, b)$  specifies the reflection element. Hence, the pre-processed phase outcome is embodied as  $\xi$  and is passed to the ensuing segmentation phase.

### 3.3. Segmenting lung nodule region by DB-UNet model

The preprocessed image  $\xi$  is considered as the input of lung nodule region segmentation, which detects and segments the accurate regions of lung nodules in the preprocessed images by using the DB-UNet system (Jian et al., 2023). DB-UNet model handles the multi-scale information, which improves the convergence and reduces the FPR as well as is flexible in nature.

#### 3.3.1. DB-UNet system

DB-UNet (Jian et al., 2023) is an enhanced version of U-Net-based CNN with the composite framework. In the structure of a multi-branch network, the two-branch encoder structure is designed, in which each branch functions independently as well as the intermediate outcomes are combined to create the last outcomes of segmentation. The Schematic outline of the DB-UNet system is designated in Fig. 2, which includes Dynamic and Depth Separable Convolution, Downsampling and Branch Fusion, and Attention Mechanism which are elucidated below.

**Dynamic and Depth Separable Convolution:** The main function of dynamic convolution is to solve the inadequate ability of the feature extraction. The convolution kernel is linked with the input image, as well as various images correspond to various convolution kernels. The exploitation of this dynamic convolution enhances the system's robustness to various databases, and also a quick rise in the entire number of parameters. By considering this, it is essential to pursue the solution for the large number of parameters produced by the outline of dynamic convolution. Particularly, the amalgamation of both dynamic and depth-separable convolution has the accuracy of parallel segmentation to the combination of both dynamic and standard convolution, but the number of parameters is minimized. In the intended architecture, the convolution kernel is considered to be  $3 \times 3$  in its corresponding dynamic branch of convolution.

**Downsampling and fusing the branch:** The down-sampling precision by kernel size  $3 \times 3$  and step size 2 of convolution is higher than the pooled down-sampling with  $2 \times 2$  kernel size. Hence, the convolution is adopted initially for down-sampling, and then, the feature information of two different branches is merged by the splicing process.

**Attention Mechanism:** In the fusion process, the low-level information in up-sampling is combined as well as the responses of irrelevant features are suppressed. Then, a novel attention module is

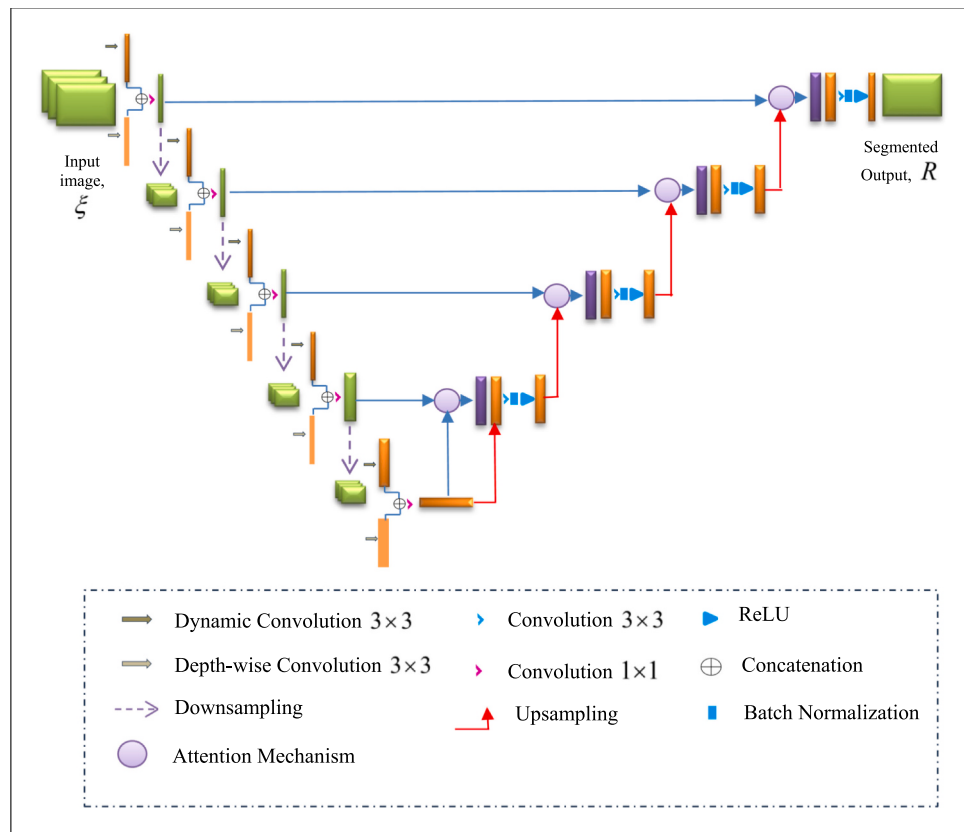


Fig. 2. Schematic outline of the DB-UNet system.

rearranged by considering the Attention UNet. Hence the segmented output obtained is indicated as  $R$ .

### 3.4. Image augmentation

The segmented output  $R$  is considered as the input for the image augmentation (Khosla and Saini, 2020) module, which is utilized to increase the range of training images through several transformations to assist in preventing the overfitting problem and enhance the ability of the system to generalize to original data. Augmentation approaches expose the model to many image variations, which allows to attain better generalizability to unseen data. Augmentation benefits to prevent the technique from overfitting for particular patterns in the training data. The reduction in overfitting issues attains better efficacy in detecting lung cancer and can lead to better performance on unseen test data. Furthermore, the augmentation process is performed through the methods of resizing, flipping, and rotating. Moreover, resizing, flipping, and rotation are employed here and are computationally inexpensive and simple to implement. Besides, these augmentation models do not require complex algorithms or additional resources for making them highly effective for augmenting large databases.

#### 3.4.1. Resizing

Resizing is a significant process, that is used to ensure that every input image possesses an even dimension and is also used creatively to simulate various perceptions to improve generalization. The resized image is specified as  $E_1$ .

#### 3.4.2. Flipping

The input image is flipped vertically or horizontally. It forms the image by rotating the image at 90 degrees. The vertical flipping is performed by tilting the image at 180 degrees, and the horizontal flipping is performed by flipping the image horizontally. Thus, the acquired output is indicated as  $E_2$ .

#### 3.4.3. Rotating

The image is tilted at 90 degrees or at tiny angles while rotating the image. After orientation, circumstantial noise is not integrated into the image when it is tilted at 90 degrees but it is not applicable when the image is tilted at minute angles. Hence, the attained rotated image is resembled as  $E_3$ .

Therefore, the outcomes of the augmented image are indicated as  $E$  and expressed as,

$$E = \{E_1, E_2, E_3\} \quad (3)$$

Therefore, the attained augmented image  $E$  is fed to the following phase.

### 3.5. Feature extraction

Feature extraction is a crucial phase to convert the image into an assessable feature, which represents the fundamental information very effectively. The augmented image  $E$  is regarded as the input for extracting features, and here, the shape-based features (Pawar et al., 2023) are extracted.

#### 3.5.1. Shape-based features

It (Pawar et al., 2023) examines the features at each pixel level that are optical in nature and possesses the properties of intuitiveness. The shape-based features, like area, perimeter, nodule solidity, and nodule irregularity index are explicated below.

i. **Nodule Perimeter:** It is defined as the property utilized to evaluate the suspicious nodule edges. If detects the distance between the adjacent pixels over the Region of Interest (RoI) and computes

the nodule edge then the perimeter returns the unknown values, and is expressed as,

$$S_1 = \sum_{m=0}^G \sum_{n=0}^D s(m, n) \quad (4)$$

where,  $G$  and  $D$  resembles the length and width of the nodule,  $s(m, n)$  specifies the values of the pixels present in the region, and  $S_1$  exemplifies the nodule perimeter.

ii. **Nodule Area:** It is termed as the irregular tissue growth in CT images and is evaluated as,

$$S_2 = \sum_{h=0}^G \sum_{j=0}^D e(h, j) \quad (5)$$

where,  $e(h, j)$  designates the pixel values in the suspicious region, and  $S_2$  implies the nodule area.

iii. **Nodule Irregularity Index:** The nodule edge is characterized by calculating the irregularity index  $S_3$  as articulated below,

$$S_3 = \frac{4\pi \times S_2}{S_1} \quad (6)$$

where,  $S_2$  and  $S_1$  denotes symbolizes the Area and perimeter of the nodule.

iv. **Nodule Solidity:** It measures the area covered under the intensity of the pixel, even though the components present in the region of the nodule are extremely focused in natural environments and is calculated as,

$$S_4 = \frac{S_1}{H} \quad (7)$$

where,  $H$  implies the Convex Hull, and  $S_4$  typifies the nodule solidity.

Henceforth, the attained shape-based features, like perimeter, area, solidity, and irregularity index are merged to generate outcomes of feature extraction that are represented as  $S$ ,

$$S = \{S_1, S_2, S_3, S_4\} \quad (8)$$

### 3.6. Lung cancer detection

Lung cancer is performed with CT images using the NAVT-Net approach, which is developed by integrating the NASNet (Cano et al., 2021) and VGG-16 (Nguyen et al., 2022). This NAVT-Net scheme comprises three elements, such as NASNet, NAVT-Net layer, and VGG-16 model. The NAVT-Net technique is a DL approach, which is employed for the detection of lung cancer in humans. This approach is utilized for optimizing the performance by improving the interpretability of the outcomes. Further, in NAVT-Net, the VGG-16 helps to extract the features, while NASNet enhances the architecture of the model by focusing on the most relevant features. Besides, the Taylor series, which is employed to combine the outcomes from VGG-16 and NASNet maximizes the stability and computational efficiency. Moreover, NAVT-Net is regarded as an effective and interpretable model for lung cancer detection using CT images. Further, the combination of NAVT-Net is more beneficial for achieving high performance even in complex medical images.

The process involved in detecting lung cancer is as follows: Firstly, the filtered image  $\xi$  is given as input to NASNet to attain the result  $A_1$ , and then fed to the NAVT-Net layer along with the mined features  $S$  for acquiring the outcomes  $A_2$  by performing the fusion process. The fusion is done by combining the NASNet and VGG-16. Further, the output of the NAVT-Net layer  $A_2$  is fed to the VGG-16 model to acquire the outcome  $A_3$ . The perspective structure of the NAVT-Net technique is deliberated in Fig. 3.

#### 3.6.1. NASNet model

Initially, the pre-processed image  $\xi$  is passed as an input to the NASNet model (Cano et al., 2021), which has high flexibility and

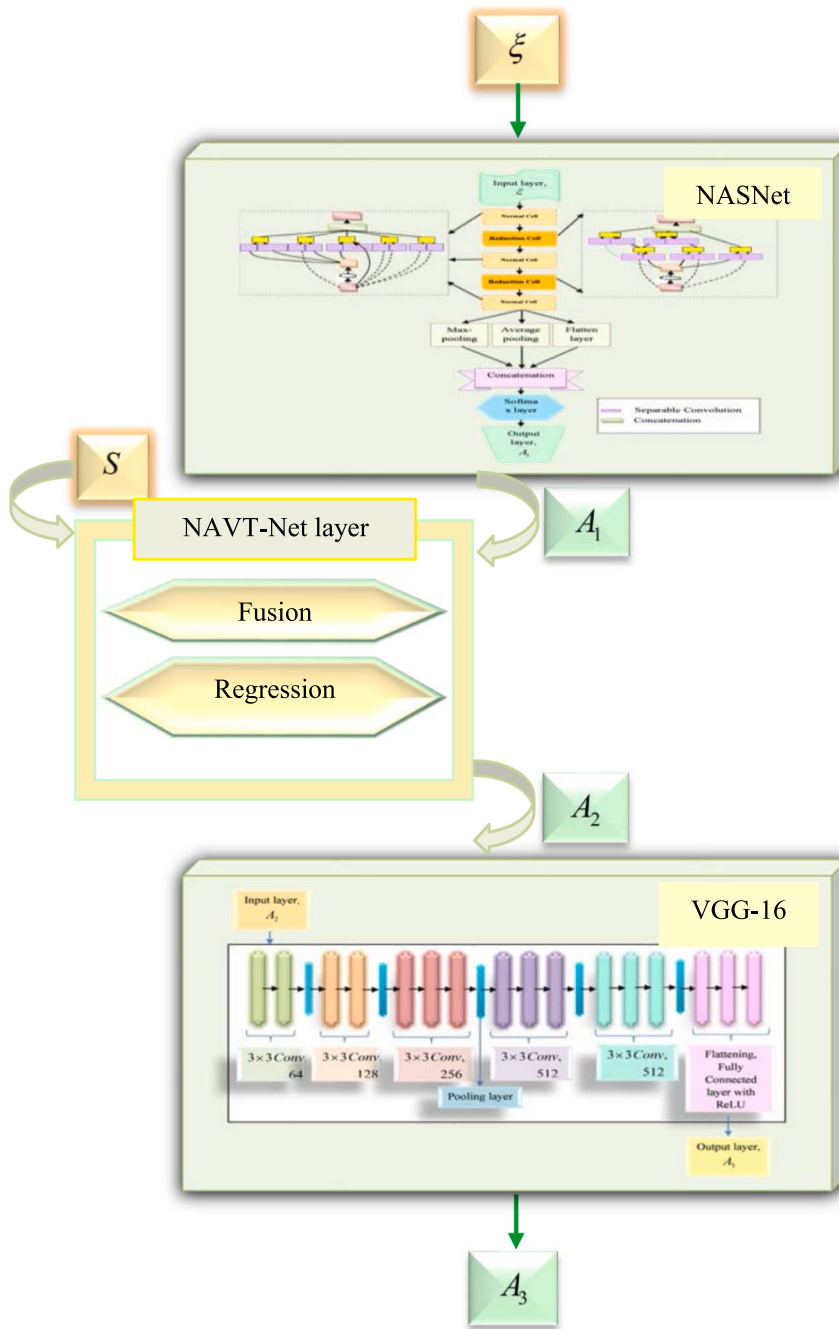


**Fig. 3.** Perspective view of the NAVT-Net technique.

scalability, increased interpretability, and improved generalization. The framework of the NASNet model is designated in Fig. 4. The collection of convolutional cells in the NASNet model includes both the normal and reduction cells that are referred to as the major functions. Normal cell returns the feature map with similar input dimensions. Likewise, the width as well as the height of the feature map with factor two is returned using the reduction cell. Subsequently, the outcomes of these layers are concatenated in the concatenate layer, which is then passed to the dropout layer that prevents the problems of network overfitting by turning off a few neurons. Consequently, the outcome from the dropout layer is furthered to the dense layer, which provides the inference to the system by the softmax function and generates the result as  $A_1$ . The utilized softmax function is expressed as,

$$A_1 = \Omega(\xi) \quad (9)$$

where, the activation function is indicated as  $\Omega$ , in which it is formulated as,

$$\Omega(\xi) = \frac{e^\xi}{\sum_{o=1}^W e^{\xi_o}} \quad (10)$$

where, the whole number of labels are implied as  $W$ , the exponential operation is typified as  $e$ , and  $\sum^\xi$  delineates probability distribution.

Consider two metrics, such as  $H$  and  $K$  be the cancer image and its corresponding label of the class. Then, the target operation  $w : H \rightarrow K$  signifies the finite point of aggregation  $w(H^1), \dots, w(H^8)$  that is considered as the known object labels as  $H^1, \dots, H^8$ , in which  $H$  is divided into several classes in accordance with the lung cancer disease. When the one-hot encoding is applied then the classes of lung cancer are

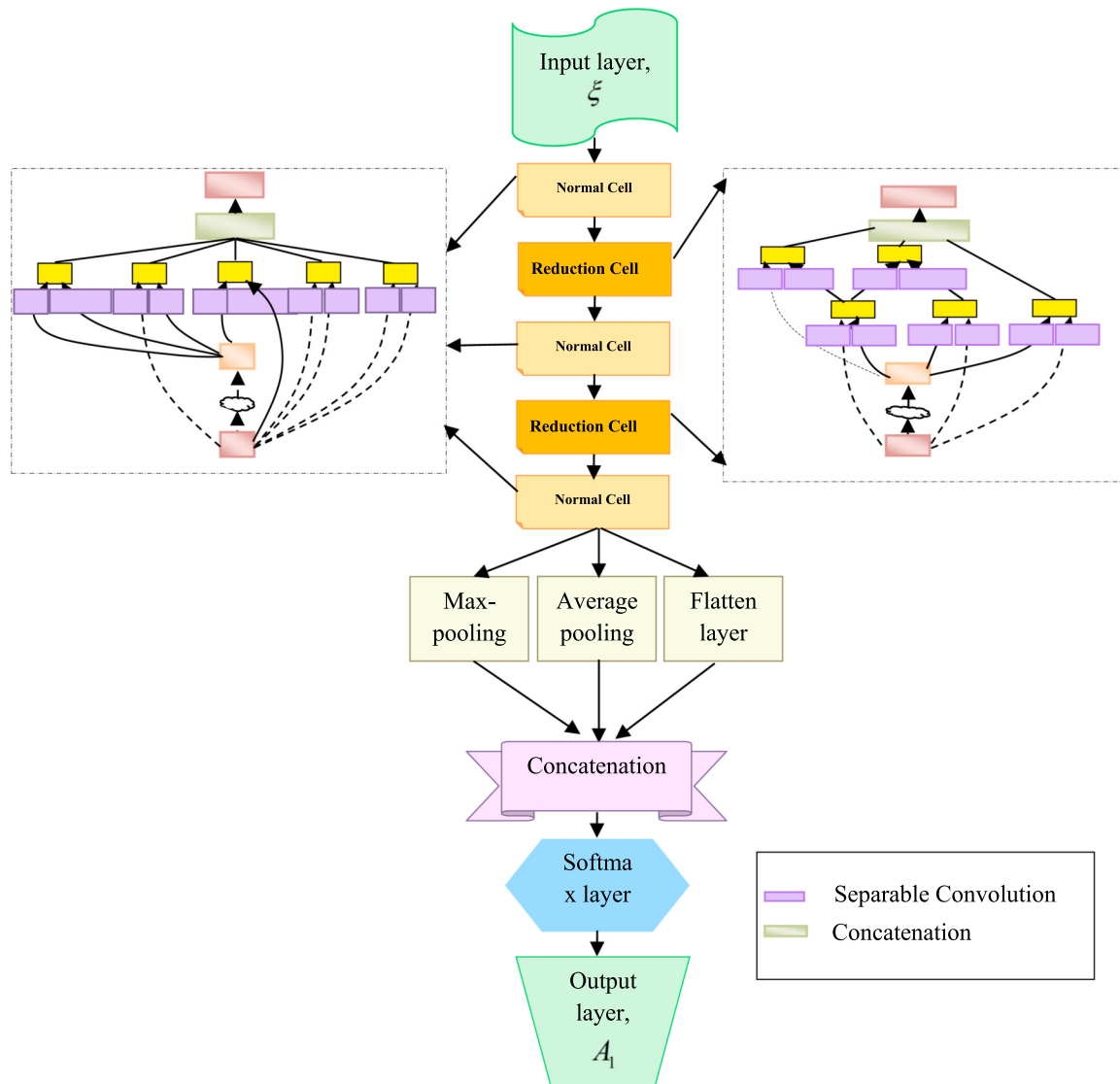


**Fig. 4.** Structural view of the NASNet model.

represented as  $Y_1, \dots, Y_8$ , which is expressed as,

$$Y_q \{t \in H | w(t) = q\} \text{ at } q \in \{1, \dots, 8\} : H = \bigcup_{q=1}^8 Y_q \quad (11)$$

Later, the target operation  $w : H \rightarrow K$  differentiates between several labels of the class is expressed as,

$$A_1 = \Omega \left( \sum_{\gamma=1}^8 \eta_{d\gamma}^3 \xi + \lambda_d^3 \right) \quad (12)$$

where,  $\gamma$  and  $d$  indicates the representation of columns and rows,  $\eta_{d\gamma}^3$  denotes the weight of  $\mathfrak{I}^{th}$  layer,  $\lambda_d^3$  signifies bias at  $\mathfrak{I}^{th}$  layer. The above Eq. (12) is vectorized as,

$$A_1 = \Omega \left( \sum_b \eta^3 * \xi + \lambda^3 \right) \quad (13)$$

Henceforth, the result of the NASNet model  $A_1$  represented in Eq. (13) is subjected to the NAVT-Net layer.

### 3.6.2. NAVT-net layer

The final outcomes from the NASNet model  $A_1$  with the extracted features  $S$  are fed as an input to the NAVT-Net layer, where they are fused

through the regression model that is done through the Taylor Series (Mangai et al., 2014). Taylor Series optimizes the functions more effectively and estimates the error in the approximation depending on the time intervals.

By considering time  $\varphi$ , the output acquired using extracted shape-based features is embodied as  $U_1$  and is expressed as,

$$U_1 = \sum_{\zeta=1}^4 S_\zeta * \Psi_\zeta \quad (14)$$

where,  $S$  represents the mined features,  $\zeta$  denotes the size of the mined features, and weight is specified as  $\Psi$ .

By applying the Taylor Series,

$$l(\varphi + 1) = l(\varphi) + \frac{l'(\varphi)}{1!} \quad (15)$$

where,

$$l(\varphi) = \frac{l(\varphi) - l(\varphi - z)}{z} \quad (16)$$

When  $z = 1$  in Eq. (16),

$$l(\varphi) = l(\varphi) - l(\varphi - 1) \quad (17)$$

By substituting the Eq. (17) in Eq. (15),

$$l(\varphi + 1) = l(\varphi) + l(\varphi) - l(\varphi - 1) \quad (18)$$

$$l(\varphi + 1) = 2l(\varphi) - l(\varphi - 1) \quad (19)$$

Consider,  $l(\varphi + 1) = A_2$ ,  $l(\varphi) = U_1$ , and  $l(\varphi - 1) = A_1$  in Eq. (19), then  $A_2 = 2U_1 - A_1$  such that Eq. (19) becomes,

$$A_2 = 2 * \left( \sum_{\xi=1}^4 S_\xi * \Psi_\xi \right) - \Omega \left( \sum_v \eta^3 * \xi + \lambda^3 \right) \quad (20)$$

The above equation yields the results of the NAVT-Net layer, which is fed to the final component of the developed NAVT-Net model namely the VGG-16 model.

### 3.6.3. VGG-16 model

The outcomes of the NAVT-Net layer  $A_2$  are the input for the VGG-16

$$A_3 = \hbar \left( V_{p_k} \dots \Xi \left( V_1 F \left\{ \varpi_{p_{con}} \Theta_{p_{con}} \times \left( \left[ \dots \left[ \varpi_2 \Theta_2 \left( \left[ \left[ 2 \left( \sum_{\xi=1}^4 S_\xi * \Psi_\xi \right) - \Omega \left( \sum_v \eta^3 * \xi + \lambda^3 \right) \right] Q_2 \right] \dots \right]^{h_{p_{con}}} Q_{p_{con}} \right) \right] \dots \right) \right\} \dots \right) \right) \quad (28)$$

model. The framework of the VGG-16 (Nguyen et al., 2022) is simple and uniform with  $3 \times 3$  filter size at the convolutional layers. The simple nature of the VGG-16 makes the system easy to implement. The depth of the VGG-16 model permits it to learn the complex features. VGG-16 model improves the performance of the entire system with filters of dimension  $3 \times 3$  and permits to capture the fine description of the image. VGG-16 model is the CNN with 16 layers, which comprises 13 layers of convolution, 3 Fully Connected layers (FCL) as well as max-pooling layers at the dimension of  $2 \times 2$  with the stride of 2. The Schematic diagram of VGG-16 is demonstrated in Fig. 5.

The deep CNN includes several convolutional layers as well as FCL as  $p_{con}$  and  $p_k$ . The width and height of the convolutional layers are represented as  $p_y$ , the number of channels at the input is denoted as  $p_{cy}$ , amount of filters is specified as  $p_{fy}$ , the height, as well as the width of output after the convolution function, is denoted as  $x_y$ , and the stride of the function is signified as  $r_y$ . The output volume of the convolutional layer  $y$  is evaluated by,

$$Z_{y+1} = \rho \left( \Theta_y \left( Z_y^{h_y} Q_y \right) \right) = \varpi_y \Theta_y \left( Z_y^{h_y} Q_y \right); \text{ for } y = 1 \dots p_{con} \quad (21)$$

where,  $Z_{y+1}$  represents the  $(y+1)^{th}$  convolutional layer, the input volume  $Z_y$  is varied from the matrix based on the filter-dependent  $Z_y^{h_y}$ . The convolutional layer does not possess the pooling function,  $\varpi_y$  signifies the identity matrix,  $\rho$  signifies the pooling operation, and  $Q_y$  resembles the filter's weight matrix. The final convolutional layer  $X_{p_{con}}$  is expressed as,

$$X_{p_{con}} = \rho \left( \Theta_{p_{con}} \left( Z_{p_{con}}^{h_{p_{con}}} Q_{p_{con}} \right) \right) \quad (22)$$

$$X_{p_{con}} = \varpi_{p_{con}} \Theta_{p_{con}} \left( Z_{p_{con}}^{h_{p_{con}}} Q_{p_{con}} \right) \quad (23)$$

The function of flattening occurs and the input of the FCL  $F$  is estimated as,

$$\Xi = F \left\{ X_{p_{con}} \right\} \quad (24)$$

Substituting Eq. (23) in Eq. (24),

$$\Xi = F \left\{ \varpi_{p_{con}} \Theta_{p_{con}} \left( Z_{p_{con}}^{h_{p_{con}}} Q_{p_{con}} \right) \right\} \quad (25)$$

Therefore, the CNN output is evaluated as,

$$T_{CNN} = \Xi_{p_k} \left( V_{p_k} \dots \Xi_2 \left( V_2 \Xi_1 \left( V_1 \Xi \right) \dots \right) \right) \quad (26)$$

where,  $V_y$  denotes the weight, as well as  $\Xi_y$  indicates the activation function of vector at FCL $y$ . Hence, the entire outcomes of the VGG-16 model is expressed as,

$$A_3 = \hbar \left( V_{p_k} \dots \Xi \left( V_1 F \left\{ \varpi_{p_{con}} \Theta_{p_{con}} \times \left( \left[ \dots \left[ \varpi_2 \Theta_2 \left( \left[ \left[ 2 \left( \sum_{\xi=1}^4 S_\xi * \Psi_\xi \right) - \Omega \left( \sum_v \eta^3 * \xi + \lambda^3 \right) \right] Q_2 \right] \dots \right]^{h_{p_{con}}} Q_{p_{con}} \right) \right] \dots \right) \right\} \dots \right) \right) \quad (27)$$

By substituting Eq. (20) in Eq. (27),

Eq. (28) exemplifies the final output of the VGG-16 model that is exemplified as  $A_3$ , and this equation designates the output of the NAVT-Net system.

## 4. Results and discussion

The efficiency of the NAVT-Net system for detecting lung cancer with CT images is analyzed with several metrics.

### 4.1. Experimental setup

The lung cancer detection using the NAVT-Net approach is executed with the Python tool. Furthermore, the size of the dataset includes 928 images, where 834 images are regarded as training samples and 93 images are considered as testing samples. Moreover, the simulation parameters of NASNet and VGG-16 methods are represented in Table 1 and Table 2.

### 4.2. Database explanation

The Figshare dataset (Classification, 2024) integrated intelligent system provides the best outcomes between input prediction systems, enhancing and boosting the efficacy of the entire system, therefore allowing better diagnosis for the patient by doctors. This database comprises the testing and training data, in which the test data encompasses 54, 120, 51, and 90 images of normal, adenocarcinoma, large cell carcinoma, as well as squamous cell carcinoma, whereas the train data contains 148 Normal images, 195 adenocarcinoma images, 115 and 155 of large cell carcinoma and squamous cell carcinoma.

### 4.3. Performance measures

The performance of the NAVT-Net is evaluated through concerning performance measures, like accuracy, TPR, TNR, F1-score, and precision.

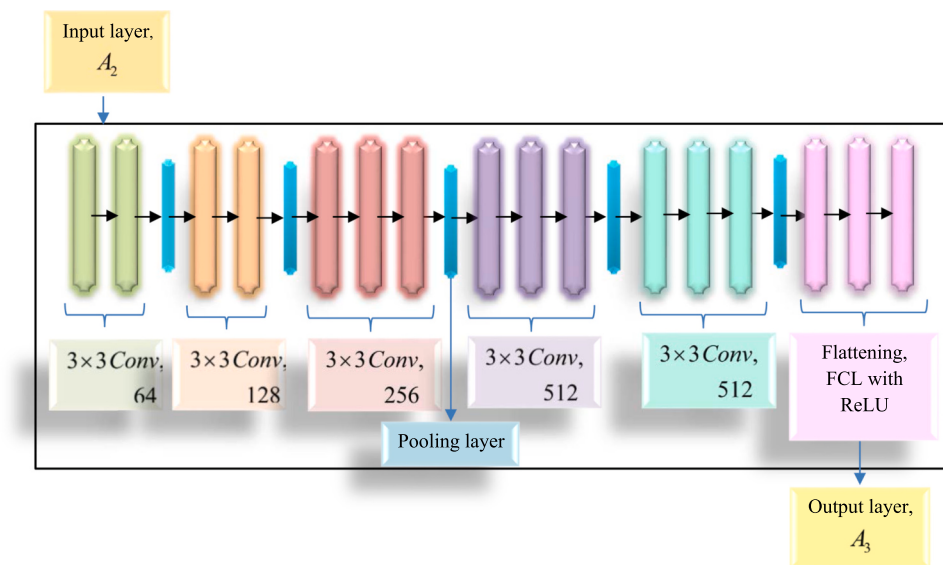


Fig. 5. Schematic diagram of VGG-16.

- i) **Accuracy:** It is referred to as the ratio of total true detection from the complete detection that is expressed as,

$$I_1 = \frac{J_1 + J_2}{J_1 + J_2 + J_3 + J_4} \quad (29)$$

where, the accuracy is designated as \$I\_1\$, \$J\_1\$ represents the True positive, \$J\_2\$ denotes the True negative, \$J\_3\$ represents the False positive, and \$J\_4\$ denotes the False negative.

- ii) **TPR:** The ability of NAVT-Net to detect the positive instances from the complete number of positive labels is termed TPR and is expressed as,

$$I_2 = \frac{J_1}{J_1 + J_4} \quad (30)$$

where, \$I\_2\$ indicates the TPR.

- iii) **TNR:** The ability of NAVT-Net to detect the negative labels from the whole number of negative samples is TNR and is deliberated below,

$$I_3 = \frac{J_2}{J_2 + J_3} \quad (31)$$

where, \$I\_3\$ specifies the TNR.

- iv) **Precision:** It states that the quantity of correctly recognized positive cases to the whole amount of lung cancer detected as positive. Moreover, precision is expressed as,

$$\text{Precision} = \frac{J_1}{J_1 + J_2} \quad (32)$$

- v) **F1-score:** It is used to evaluate the performance of the NAVT-Net technique successfully. Besides, it is also exploited to fuse recall

and precision and recall into a single score for offering an entire valuation, and it is specified as,

$$\text{F1-score} = \frac{2 \times \text{Precision} \times \text{Recall}}{\text{Precision} + \text{Recall}} \quad (33)$$

#### 4.4. Experimental outcomes

The NAVT-Net for lung cancer detection obtained the image results for both normal and lung cancer images.

##### (i) Normal image

The experimental outcomes for normal images using NAVT-Net are expounded in Fig. 6. Fig. 6a) explicates the input image, the pre-processed image is illustrated in Fig. 6b), and Fig. 6c) and 6d) deliberates the segmented and detected image.

##### (ii) Lung cancer image

The experimental consequences of the lung cancer image using NAVT-Net are explicated in Fig. 7. Fig. 7a) specifies the input image, the preprocessed image is revealed in Fig. 7b), as well as the segmented and detected image is depicted in Fig. 7c) and 7d).

#### 4.5. Performance validation

The efficacy of the NAVT-Net model is evaluated based on the training samples by changing the number of layers and epochs.

##### i) Validation by varying layers

Fig. 8 illustrates the assessment of the NAVT-Net with training samples by differing the layers. Fig. 8(a) demonstrates the assessment of NAVT-Net related to accuracy. The accuracy gained for 2, 4, 6, and 8 layers by the NAVT-Net with 90 % training samples is 87.168 %, 88.979 %, 90.979 %, and 91.858 % respectively. The investigation of NAVT-Net concerning TPR is illustrated in Fig. 8(b). The TPR achieved by NAVT-Net with the number of layers, such as 2, 4, 6, and 8, is 88.000 %, 89.279 %, 92.000 %, and 93.465 % with 90 % training

**Table 1**  
Simulation parameter of NASNet.

Parameter	Values
Epoch	20
Batch size	16
Loss	Binary cross entropy
Optimizer	Adam
Learning rate	0.001

**Table 2**  
Simulation parameter of VGG-16.

Parameter	Values
Epoch	10
Batch size	32
Loss	Binary cross entropy
Optimizer	Adam
Learning rate	0.001

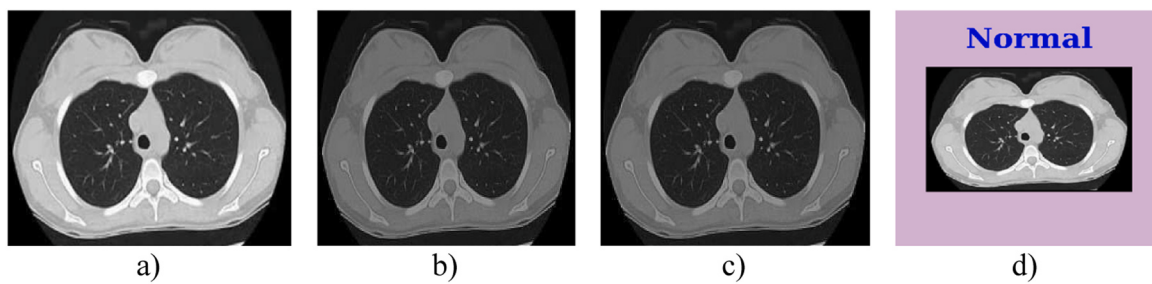


**Fig. 6.** Experimental Results of the normal image using NAVT-Net: a) input image b) preprocessed image c) segmented image, d) Detected image.

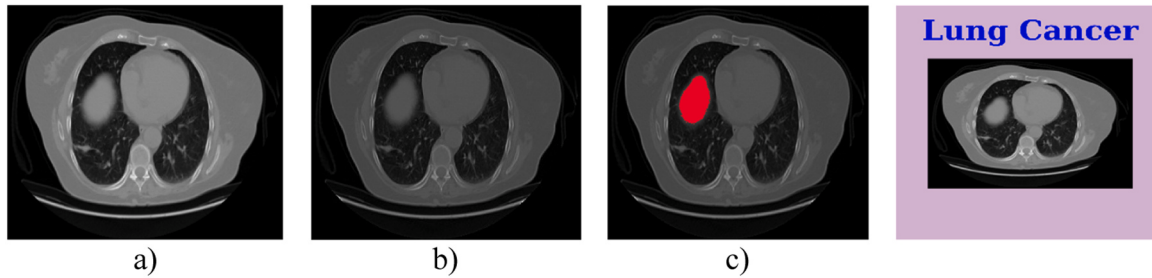


**Fig. 7.** Experimental Outcomes of lung cancer image using NAVT-Net: a) input image b) preprocessed image c) segmented image, d) Detected image.

samples. **Fig. 8(c)** reveals the TNR-based examination by NAVT-Net. At 90 % of training samples, the TNR recorded by applying the NAVT-Net at 2, 4, 6, and 8 layers is 86.798 %, 88.876 %, 90.008 %, and 91.457 % correspondingly. In **Fig. 8(d)**, the assessment of NAVT-Net with F1-score is represented. For the training sample 70 %, the F1-score recorded by NAVT-Net for 2, 4, 6, and 8 layers are 83.056 %, 85.980 %, 87.282 %, and 88.998 %. The precision-based evaluation of NAVT-Net is signified in **Fig. 8(e)**. At training sample 60 %, the precision quantified by NAVT-Net for 2, 4, 6, and 8 layers are 80.846 %, 82.178 %, 83.996 %, and 85.145 %.

#### *ii) Validation by differing epochs*

The valuation of the NAVT-Net with training samples by changing the epochs is indicated in **Fig. 9**. The appraisal of NAVT-Net with accuracy is demonstrated in **Fig. 9(a)**. The accuracy attained by utilizing the NAVT-Net at training samples 90 % for epochs 10, 20, 30, and 40 is 85.679 %, 87.546 %, 89.990 %, and 91.858 % respectively. The examination of NAVT-Net with TPR is demonstrated in **Fig. 9(b)**. The TPR achieved using NAVT-Net with epochs, such as 10, 20, 30, and 40 is 86.677 %, 88.769 %, 91.891 %, and 93.465 % with training samples 90 %. **Fig. 9(c)** signifies the TNR-based analysis of the NAVT-Net. At 90 % of training samples, the TNR acquired by the NAVT-Net for epochs 10, 20, 30, and 40 is 85.788 %, 87.677 %, 89.899 %, and 91.457 %. The F1-score-based evaluation of NAVT-Net is signified in **Fig. 9(d)**. At training sample 70 %, the F1-score quantified by NAVT-Net for 2, 4, 6, and 8 layers are 83.896 %, 85.275 %, 87.006 %, and 88.178 %. In **Fig. 9(e)**, the assessment of NAVT-Net with precision is represented. For the training sample 80 %, the precision recorded by NAVT-Net for 2, 4, 6, and 8 layers are 81.766 %, 83.777 %, 85.006 %, and 86.178 %.

#### 4.6. Comparative approaches

The comparative schemes for the assessment of the NAVT-Net in lung cancer detection are EfficientNetB1-Lung-EffNet (Raza et al., 2023), 3D analysis (Said et al., 2023), MENet (Majumder et al., 2024), and VER-Net (Saha et al., 2024).

#### 4.7. Comparative validation

The efficacy of the NAVT-Net system is compared with different

approaches at varying training samples and K-values and this is deliberated below.

##### *(i) With Training Samples*

The comparative investigation of NAVT-Net concerning training samples is elucidated in **Fig. 10**. **Fig. 10 (a)** reveals the accuracy-based validation of NAVT-Net based on training samples. The EfficientNetB1-Lung-EffNet acquired an accuracy of 83.279 %, 3D analysis attained 85.009 %, MENet acquired 87.566 %, VER-Net reached 89.278 %, and developed NAVT-Net achieved 91.858 % with training samples 90 %. The accuracy of the devised NAVT-Net is improved by 2.80 % when compared to the VER-Net system. The comparative validation of NAVT-Net with TPR is deliberated in **Fig. 10 (b)**. At training samples of 90 %, the prevailing schemes including EfficientNetB1-Lung-EffNet, 3D analysis, MENet, VER-Net, and developed NAVT-Net attained the TPR of 84.568 %, 86.135 %, 88.788 %, 91.000 %, and 93.465 %. The TPR by introduced NAVT-Net is higher by 5.00 % when compared with the MENet scheme. Besides, the valuation of NAVT-Net with TNR is revealed in **Fig. 10 (c)**. At the training sample of 90 %, the traditional schemes, like EfficientNetB1-Lung-EffNet, 3D analysis, MENet, VER-Net, as well as the devised NAVT-Net achieved the TNR of 81.348 %, 84.007 %, 86.677 %, 88.988 %, and 91.457 % accordingly. Therefore, the TNR of NAVT-Net is 8.146 % better than the 3D analysis. **Fig. 10(d)** signifies the evaluation of NAVT-Net on the basis of the F1-score. Here, for the training sample 80 %, the F1-score calculated by NAVT-Net is 88.178 %, while the other models, like EfficientNetB1-Lung-EffNet, 3D analysis, MENet, and VER-Net figured a F1-score of 79.998 %, 82.034 %, 83.888 %, and 86.178 %. Here, the performance of NAVT-Net is improved by 9.28 %, 6.97 %, 4.87 %, and 2.27 %. The examination of NAVT-Net concerning precision is exemplified in **Fig. 10(e)**. At training sample 90 %, the NAVT-Net, EfficientNetB1-Lung-EffNet, 3D analysis, MENet, and VER-Net measured a precision of 91.279 %, 81.970 %, 83.570 %, 87.699 %, and 89.285 %. Moreover, the performance enhancement of NAVT-Net is 10.20 %, 8.45 %, 3.92 %, and 2.18 %. **Fig. 10(f)** displays the graph between consumption time and training samples. At training sample 80 %, the consumption time calculated by EfficientNetB1-Lung-EffNet, 3D analysis, MENet, VER-Net, and NAVT-Net is 77.688 s, 69.788 s, 55.885 s, 38.997 s, and 31.486 s. In **Fig. 10(g)**, the valuation of NAVT-Net regarding memory usage is illustrated. For the training sample of

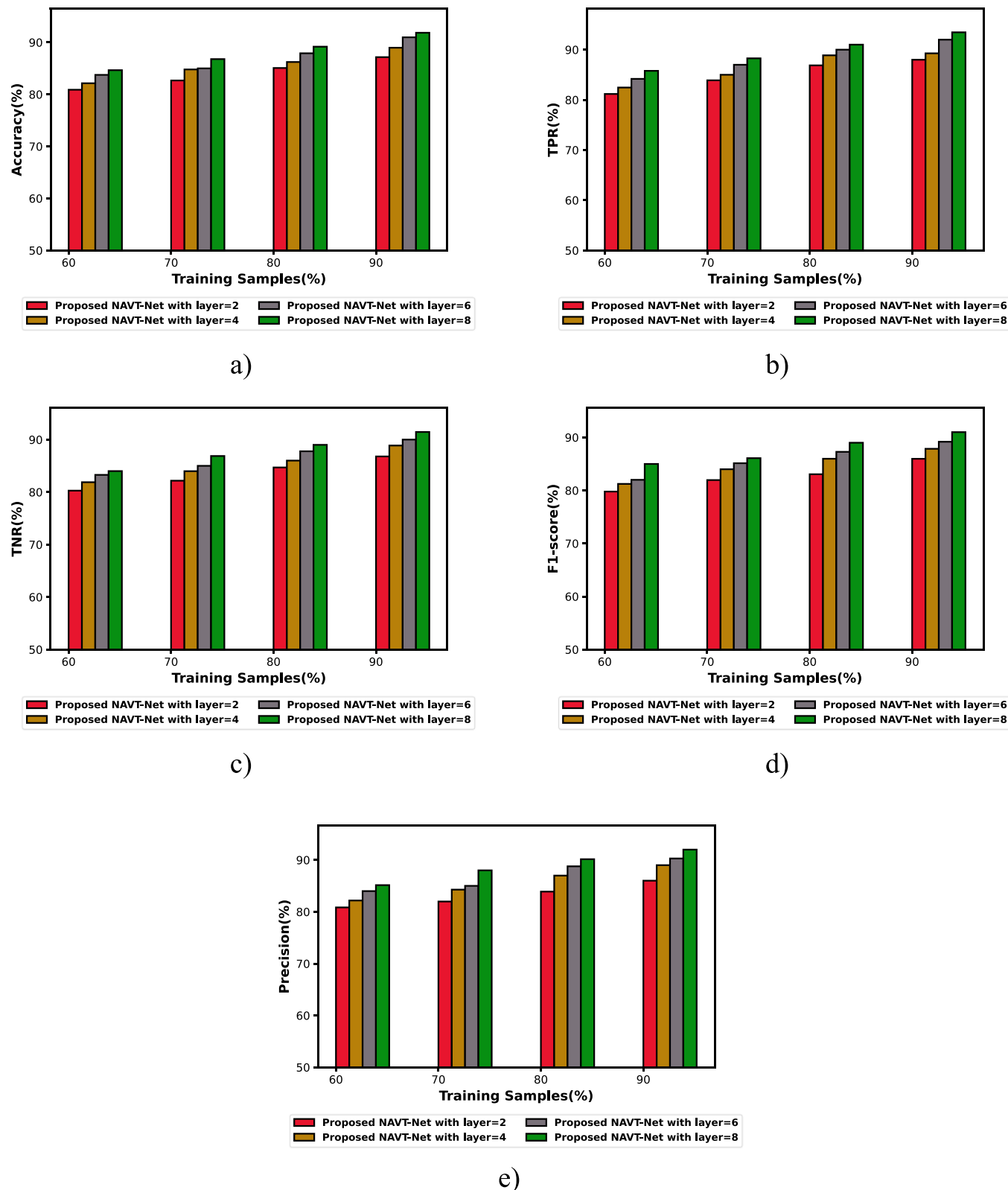


**Fig. 8.** Performance validation by varying layers with training samples a) accuracy b) TPR c) TNR, TPR d) F1-score, e) Precision.

60 %, the NAVT-Net measured a memory usage of 34.800MB, while the prevailing methods including EfficientNetB1-Lung-EffNet, 3D analysis, MENet, and VER-Net attained a memory usage of 42.900MB, 39.900 M, 37.200MB, and 36.200MB.

#### ii) With K-Value

The comparative appraisal of NAVT-Net concerning K-values is elucidated in Fig. 11. The comparative analysis of accuracy achieved by NAVT-Net is exposed in Fig. 11 (a). With K-values 9, the prior schemes including EfficientNetB1-Lung-EffNet, 3D analysis, MENet, VER-Net, and established NAVT-Net recorded accuracy of 84.99 %, 86.179 %,

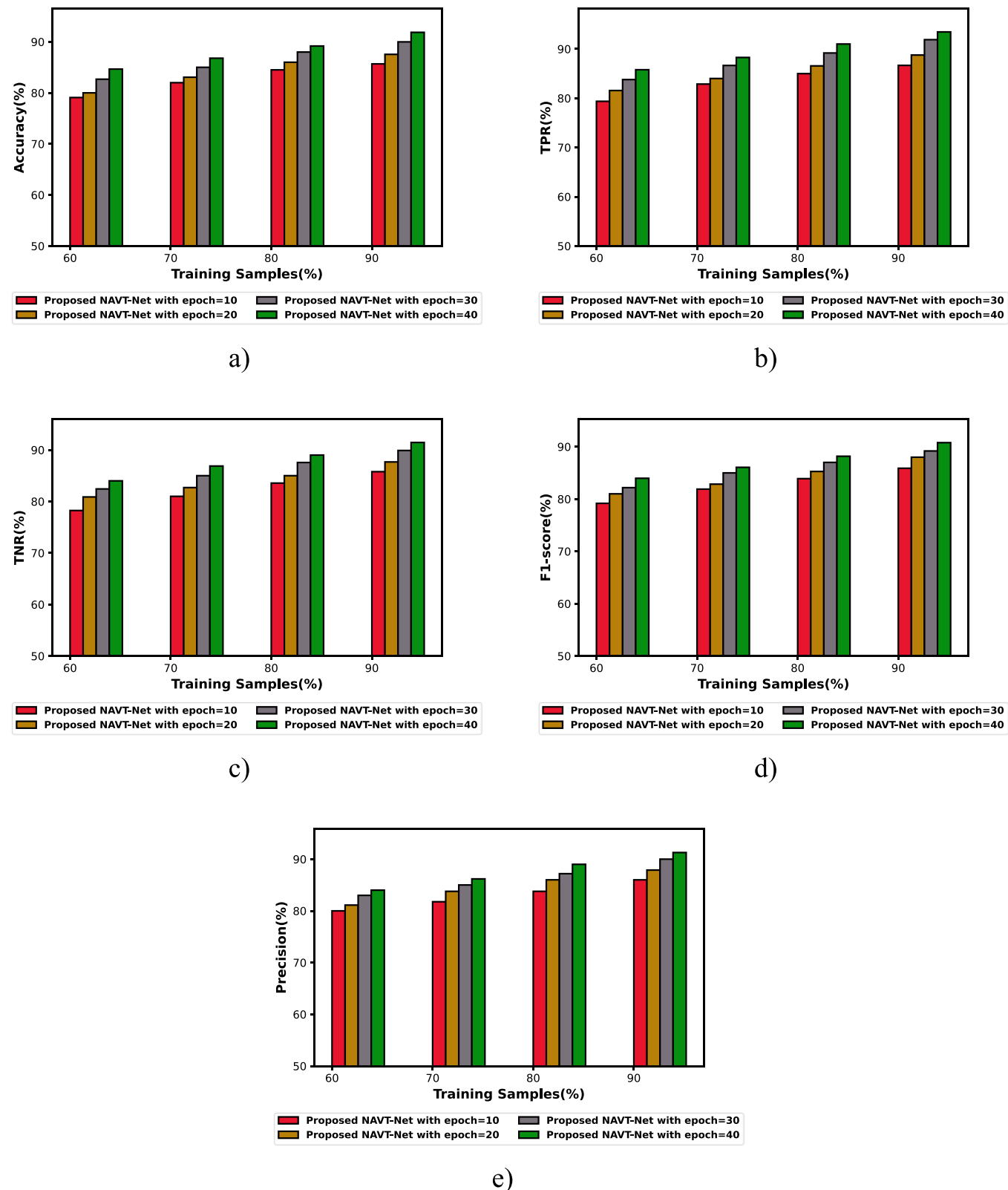


**Fig. 9.** Performance validation by varying epochs with training samples a) accuracy b) TPR c) TNR, TPR d) F1-score, Precision.

88.979 %, 90.006 %, and 92.176 %. The accuracy obtained using NAVT-Net is raised by 2.35 % when compared with the system of MENet. Moreover, the TPR-based assessment of NAVT-Net is exhibited in Fig. 11 (b). By K-value of 9, the conventional systems including EfficientNetB1-Lung-EffNet, 3D analysis, MENet, VER-Net, and

proposed NAVT-Net attained the TPR of 85.005 %, 87.000 %, 89.879 %, 91.879 %, and 93.997 % accordingly. Hence, the TPR value of NAVT-Net is 4.38 % superior to 3D analysis. Fig. 11 (c) shows the TNR value achieved by NAVT-Net based on K-value. The EfficientNetB1-Lung-EffNet reached an TNR of 82.454 %, 3D analysis attained 85.679 %,

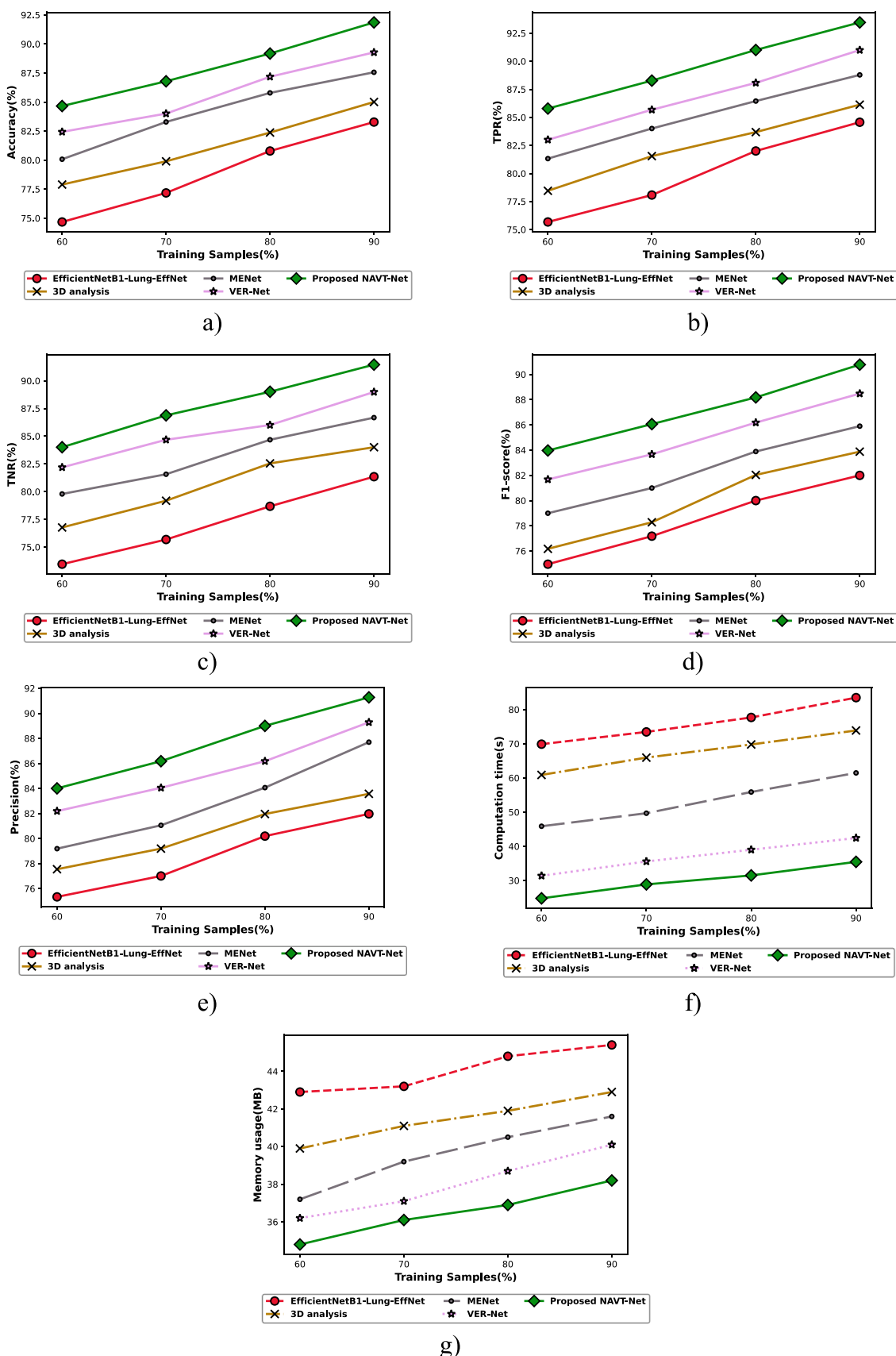


**Fig. 10.** Comparative evaluation with training samples by NAVT-Net: a) accuracy b) TPR c) TNR, TPR d) TNR, e) F1-score, Precision, f) Computation time, g) Memory usage.

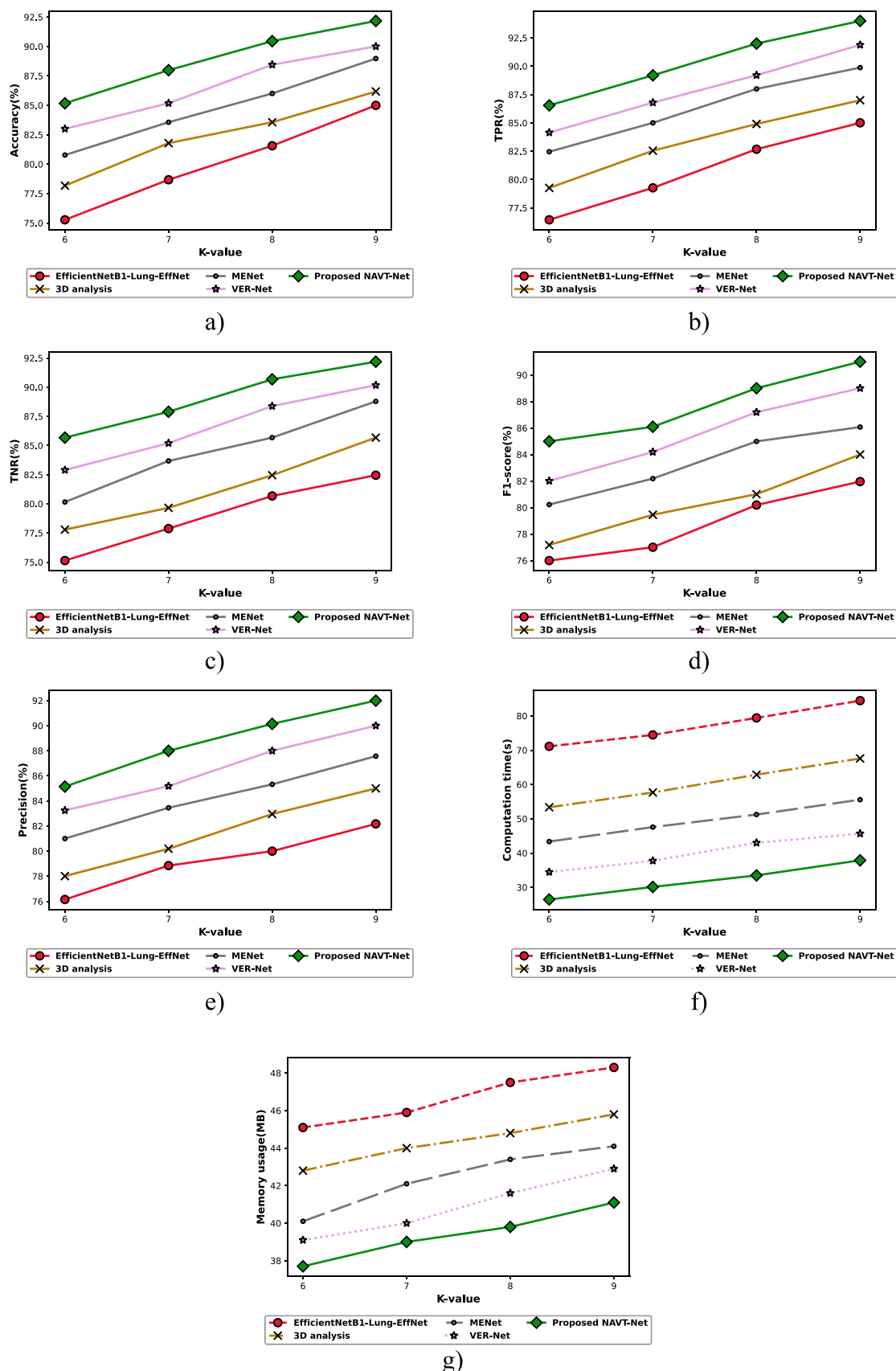


**Fig. 11.** Comparative validation with K-Values by NAVT-Net: a) accuracy b) TPR c) TNR d) F1-score, Precision, f) Computation time, g) Memory usage.

MENet acquired 88.788 %, VER-Net reached 90.178 %, and developed NAVT-Net achieved 92.1789 % with K-value 9. The TNR achieved by the introduced NAVT-Net is raised by 7.06 % when compared to the VER-Net. The examination of NAVT-Net concerning F1-score is exemplified in Fig. 11(d). At k-value 8, the NAVT-Net, EfficientNetB1-Lung-EffNet, 3D analysis, MENet, and VER-Net measured a F1-score of 89.998 %, 80.188 %, 81.007 %, 84.990 %, and 87.187 %. Fig. 11(e) signifies the evaluation of NAVT-Net on the basis of precision. Here, for k-value 6, the precision calculated by NAVT-Net is 85.145 %, while the other models, like EfficientNetB1-Lung-EffNet, 3D analysis, MENet, and VER-Net figured a precision of 76.145 %, 78.007 %, 80.999 %, and 83.245 %. Fig. 11(f) displays the graph between consumption time and k-value. At k-value 7, the consumption time calculated by EfficientNetB1-Lung-EffNet, 3D analysis, MENet, VER-Net, and NAVT-Net is 74.458 s, 57.676 s, 47.568 s, 37.757 s, and 30.122 s. In Fig. 11(g), the valuation of NAVT-Net regarding memory usage is illustrated. For k-value 8, the NAVT-Net measured a memory usage of 39.800MB, while the prevailing methods including EfficientNetB1-Lung-EffNet, 3D analysis, MENet, and VER-Net attained a memory usage of 47.500MB, 44.800MB, 43.400MB, and 41.600MB.

#### 4.8. ROC analysis

The Region of Convergence (ROC) curve is employed to detect the perfect threshold value and improves the entire performance of the classifier. The prediction outcomes of a confusion matrix at each point are specified in the ROC space, and the curve is plotted between the False Positive Rate (FPR) and TPR. Fig. 12 represents the ROC valuation of the NAVT-Net concerning TPR by adjusting FPR. With the Consideration of FPR as 0.8, the TPR attained by EfficientNetB1-Lung-EffNet is 0.947, 3D analysis is 0.970, MENet is 0.970 and VER-Net is 0.981, whereas the introduced NAVT-Net achieved the TPR of 0.995.

#### 4.9. Comparative discussion

Table 3 demonstrates the comparative discussion of NAVT-Net regarding various evaluation measures. The table explains that the developed NAVT-Net reached the highest values of accuracy, TPR, TNR, F1-score, precision, computational time, and memory usage of 92.176 %, 93.997 %, and 92.189 %, 90.999 %, and 91.998 %, 37.879 s, and 41.100MB for K-value 9. The accuracy recorded with the schemes, such as EfficientNetB1-Lung-EffNet, 3D analysis, MENet, and VER-Net is 84.999 %, 86.179 %, 88.979 %, and 90.006 %. The TPR attained by the prevailing techniques, like EfficientNetB1-Lung-EffNet is 85.008 %, 3D analysis is 87.000 %, MENet is 89.879 %, and VER-Net is 91.879 %. Furthermore, the conventional approaches, like EfficientNetB1-Lung-

EffNet, 3D analysis, MENet, and VER-Net obtained the TNR of 82.454 %, 85.679 %, 88.788 %, and 90.178 %. Furthermore, the value of the F1-score quantified by EfficientNetB1-Lung-EffNet, 3D analysis, MENet, and VER-Net is 81.957 %, 83.998 %, 86.068 %, and 88.997 %, while these methods obtained a precision of 82.173 %, 84.998 %, 87.569 %, and 90.000 %. In addition to this, the computational time calculated by other prevailing approaches are 84.459 s, 67.585 s, 55.565 s, and 45.677 s, while the aforementioned approaches figured a memory usage of 48.300MB, 45.800MB, 44.100MB, and 42.900MB. Hence, NASNet enhances the interpretability and minimizes the computational complexity, as well as it is scalability in nature. VGG-16 is stable in training and improves performance since it is strong enough. Thus, the amalgamation of NASNet and VGG-16 improves the total performance of the entire scheme while detecting lung cancer.

#### 4.10. Statistical analysis

Statistical testing is regarded as a constant technique, which is exploited to correlate the experimental outcomes. This model is used for determining if the hypothesis is supported by sample data and whether the outcomes are generalized.

- (i) **Anova test:** The main feature of this method is the F-statistic and P-value, and here P-value is utilized for quantifying the possibility, in which the attained outcomes result under the null hypothesis. Frequently, the value of the P-value is less than 0.05, and it is represented as the null hypothesis, which should be rejected. Furthermore, an ANOVA test is performed for verifying the statistical significance of the newly presented NAVT-Net approach by checking the difference among the means of multiple groups. Here, the P-value is 0.025, which is less than 0.5, and thus it leads to null hypothesis rejection. Further, the statistical significance of the enhancement in performance is confirmed, and hence the efficacy of the NAVT-Net is validated. In addition to this, ANOVA F-statistic is employed for determining the significant difference among the means of multiple groups. Here, the variation among group means to the variation within groups is compared, and a higher F-statistic value is specified as the larger probability. Further, in this paper, the value of the ANOVA F-statistic is 4.031. The ANOVA test with its values is shown in Table 4.
- (ii) **Confidence Interval (CI):** The CI is considered as a statistical range, which is utilized for estimating the true value of a population parameter. Moreover, it includes a range of values, that are computed from sample data. The value of CI is mostly expressed in percentage, and the values are portrayed in Table 5. Here, the CI value of proposed NAVT-Net is (85.40093823510756, 91.0747334289243), whereas the conventional approaches, namely EfficientNetB1-Lung-EffNet, 3D analysis, MENet, and VER-Net recorded a CI value of (76.56095170805744, 87.39738329194256), (79.47647176583907, 89.48835980106094), (79.47647176583907, 89.48835980106094), and (82.3075329140327, 90.48957642862572).

#### 4.11. Practical implications

The NAVT-Net technique significantly minimizes the time spent by radiologists on every scan report. Moreover, this model reduces the errors done by clinicians by attaining faster diagnosis, and it leads to quick treatment of disease. Further, NAVT-Net potentially helps in pre-surgical planning by offering precise regions of the tumor's boundaries, and it guides surgeons to lessen damage to the nearest healthy tissue.

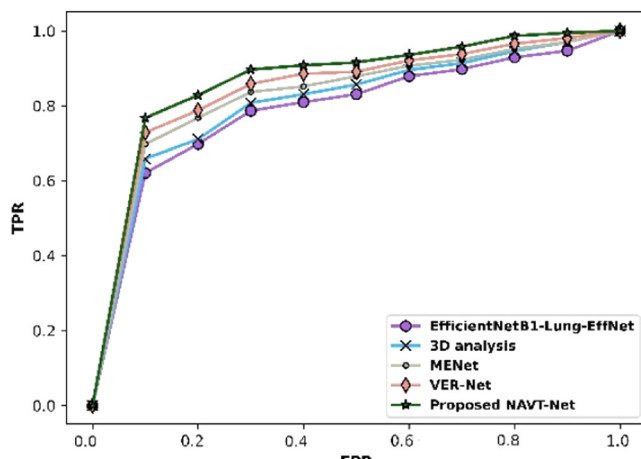


Fig. 12. ROC Valuation.

**Table 3**

Comparative discussion.

Variations	Metrics	Prior Approaches			Proposed NAVT-Net
		Figshare dataset			
K-Value	<b>Accuracy (%)</b>	84.999	86.179	88.979	90.006
	<b>TPR (%)</b>	85.008	87.000	89.879	91.879
	<b>TNR (%)</b>	82.454	85.679	88.788	90.178
	<b>F1-score (%)</b>	81.957	83.998	86.068	88.997
	<b>Precision (%)</b>	82.173	84.998	87.569	90.000
	<b>Consumption time (s)</b>	84.459	67.585	55.565	45.677
	<b>Memory usage (MB)</b>	48.300	45.800	44.100	42.900
Training Samples	<b>Accuracy (%)</b>	83.279	85.009	87.566	89.278
	<b>TPR (%)</b>	84.568	86.135	88.788	91.000
	<b>TNR (%)</b>	81.348	84.007	86.677	88.988
	<b>F1-score (%)</b>	81.996	83.877	85.899	88.479
	<b>Precision (%)</b>	81.970	83.570	87.699	89.285
	<b>Consumption time (s)</b>	83.485	73.879	61.474	42.436
	<b>Memory usage (MB)</b>	45.400	42.900	41.600	40.100
					38.200

**Table 4**  
ANOVA Test.

ANOVA F-statistic	4.0313518
ANOVA P-value	0.02592289

**Table 5**  
Confidence interval.

Methods	Values
EfficientNetB1-Lung-EffNet	(73.07114617837609, 85.56829852162392)
3D analysis	(76.56095170805744, 87.39738329194256)
MENet	(79.47647176583907, 89.48835980106094)
VER-Net	(82.3075329140327, 90.48957642862572)
Proposed NAVT-Net	(85.40093823510756, 91.0747334289243)

#### 4.12. Limitations and future works of the present study

The limitations in this manuscript are listed as: The proposed technique only detected lung cancer in humans, but failed to classify the lung cancer using CT images. Further, future work aims to execute new techniques for lung cancer classification. In addition to this, the newly devised approach attained better accuracy, TPR, TNR, F1-score, and precision values, but this approach needed computational resources for the tuning process. Besides, optimization approaches can also be implemented for training the DL networks for attaining a high performance rate. Besides, in the future, a novel AI type, labeled “explainable AI,” can be developed for enabling cooperation or balance among human intelligence and AI, which brings both technologies in compliance with legal requirements (Sorantin et al., 2021). In addition to this, the implementation of explainable AI minimizes the time required for computation with less complexity, moreover, this method has the capability to attain the results with high generalizability with more satisfactory outcomes.

#### 5. Conclusion

Lung cancer is a fatal sickness, which is to be detected at the preliminary phase to improve the existence rate of the concerned patients. In recent days, new technologies have been created to detect the disease but due to its appearance, it is regarded as a challenging task. Here, NAVT-Net is introduced for detecting lung cancer with CT images, which are collected and then preprocessed based on homomorphic filtering. Later, the preprocessed image is forwarded to the segmentation stage to detect the region of lung nodule through the DB-UNet. Thereafter, image augmentation is used to expand the size and to generalize better by minimizing the overfitting issues through resizing, flipping,

and rotating processes. Consequently, the feature extraction is done based on the shape-based features. Finally, lung cancer is detected by NAVT-Net which is established by the amalgamation of NASNet and VGG-16 with Taylor series. Hence, the NAVT-Net reached a better accuracy of 92.176 %, TPR of 93.997 %, TNR of 92.189 %, F1-score of 90.999 %, and precision of 91.998 %, computational time, and memory usage of 37.879 s, and 41.100MB for K-value 9. In addition, the future examination, numerous images will be collected from the other databases, and ensemble approaches will be utilized to attain superior results for lung cancer.

#### Author statement

The authors confirm contribution to the paper as follows: study conception and design: Lokanathan Jimson, Data collection: John Patrick Ananth analysis and interpretation of results. All authors reviewed the results and approved the final version of the manuscript.

#### CRediT authorship contribution statement

**Lokanathan Jimson:** Conceptualization, Methodology, Validation, Formal analysis, Investigation, Writing – original draft, Writing – review & editing. **John Patrick Ananth:** Resources, Visualization, Project administration

#### Declaration of Competing Interest

The authors declare that they have no known competing financial interests or personal relationships that could have appeared to influence the work reported in this paper.

#### References

- Adelsmayr, G., Janisch, M., Kaufmann-Bühler, A.K., Holter, M., Talakic, E., Janek, E., Holzinger, A., Fuchsjäger, M., Schöllnast, H., 2023b. “CT texture analysis reliability in pulmonary lesions: the influence of 3D vs. 2D lesion segmentation and volume definition by a Hounsfield-unit threshold”. Eur. Radiol. 33 (5), 3064–3071.
- Adelsmayr, G., Janisch, M., Müller, H., Holzinger, A., Talakic, E., Janek, E., Streit, S., Fuchsjäger, M., Schöllnast, H., 2023a. “Three dimensional computed tomography texture analysis of pulmonary lesions: does radiomics allow differentiation between carcinoma, neuroendocrine tumor and organizing pneumonia?”. Eur. J. Radiol. 165, 110931.
- Ahmed, T., Parvin, M.S., Haque, M.R., Uddin, M.S., 2020. Lung cancer detection using CT image based on a 3D convolutional neural network. J. Comput. Commun. 8 (03), 35.
- Alzubaidi, M.A., Otoom, M., Jaradat, H., 2021. Comprehensive and comparative global and local feature extraction framework for lung cancer detection using CT scan images. IEEE Access 9, 158140–158154.
- Asuntha, A., Srinivasan, A., 2020. Deep learning for lung cancer detection and classification. Multimed. Tools Appl. 79 (11), 7731–7762.

- Cano, E., Mendoza-Avilés, J., Areiza, M., Guerra, N., Mendoza-Valdés, J.L., Rovetto, C.A., 2021. Multi skin lesions classification using fine-tuning and data-augmentation applying NASNet. *PeerJ Comput. Sci.* 7, e371.
- Classification of Lung Cancer Computed Tomography Images dataset will be taken from “<https://figshare.com/articles/dataset/Mahesswari/23741562>”, accessed on May 2024.
- Crasta, L.J., Neema, R., Pais, A.R., 2024. A novel Deep Learning architecture for Lung cancer detection and diagnosis from Computed Tomography Image Analysis. *Healthc. Anal.* 5, 100316.
- Dewes, P., Frellesen, C., Al-Butmeh, F., Albrecht, M.H., Scholtz, J.E., Metzger, S.C., Lehnert, T., Vogl, T.J., Wichmann, J.L., 2016. Comparative evaluation of non-contrast CAIPIRINHA-VIBE 3T-MRI and multidetector CT for detection of pulmonary nodules: in vivo evaluation of diagnostic accuracy and image quality. *Eur. J. Radiol.* 85 (1), 193–198.
- Dodia, S., Basava, A., Padukudru Anand, M., 2022. A novel receptive field-regularized V-net and nodule classification network for lung nodule detection. *Int. J. Imaging Syst. Technol.* 32 (1), 88–101.
- Elnakib, A., Amer, H.M. and Abou-Chadi, F.E., “Early lung cancer detection using deep learning optimization”, 2020.
- Han, Y.T., Lin, G.J., Zhao, L.J., Tang, X.L., Huang, Y., Jiang, H., 2021. An improved homomorphic filtering algorithm for face image preprocessing. *J. Comput.* 32 (6), 66–82.
- Heuvelmans, M.A., van Ooijen, P.M., Ather, S., Silva, C.F., Han, D., Heussel, C.P., Hickes, W., Kauczor, H.U., Novotny, P., Peschl, H., Rook, M., 2021. Lung cancer prediction by deep learning to identify benign lung nodules. *Lung Cancer* 154, 1–4.
- Jian, M., Wu, R., Fu, L. and Yang, C., “Dual-branch-UNnet: A dual-branch convolutional neural network for medical image segmentation”, 2023.
- Khosla, C., Saini, B.S., 2020. Enhancing performance of deep learning models with different data augmentation techniques: a survey. *Int. Conf. Intell. Eng. Manag.* 79–85.
- Majumder, S., Gautam, N., Basu, A., Sau, A., Geem, Z.W., Sarkar, R., 2024. MENet: A Mitscherlich function-based ensemble of CNN models to classify lung cancer using CT scans. *Plos One* 19 (3), e0298527.
- Makaju, S., Prasad, P.W.C., Alsadoon, A., Singh, A.K., Elchouemi, A., 2018. Lung cancer detection using CT scan images. *Procedia Comput. Sci.* 125, 107–114.
- Mangai, S.A., Sankar, B.R., Alagarsamy, K., 2014. Taylor series prediction of time series data with error propagated by artificial neural network. *Int. J. Comput. Appl.* 89 (1).
- Nguyen, H.T., Li, S., Cheah, C.C., 2022. A layer-wise theoretical framework for deep learning of convolutional neural networks. *IEEE Access* 10, 14270–14287.
- Pawar, V.J., Premchand, P., Govardhanrao, I., 2023. Lung cancer nodules detection using ideal features extraction technique in CT images. *Proc. First Int. Conf. Adv. Comput. Vis. Artif. Intell. Technol.* 39–57.
- Raza, R., Zulfiqar, F., Khan, M.O., Arif, M., Alvi, A., Iftikhar, M.A., Alam, T., 2023. Lung-EffNet: lung cancer classification using EfficientNet from CT-scan images. *Eng. Appl. Artif. Intell.* 126, 106902.
- Saha, A., Ganie, S.M., Pramanik, P.K.D., Yadav, R.K., Mallik, S., Zhao, Z., 2024. VER-Net: a hybrid transfer learning model for lung cancer detection using CT scan images. *BMC Med. Imaging* 24.
- Said, Y., Alsheikhy, A.A., Shawly, T., Lahza, H., 2023. Medical images segmentation for lung cancer diagnosis based on deep learning architectures. *Diagnostics* 13 (3), 546.
- Shafi, I., Din, S., Khan, A., Díez, I.D.L.T., Casanova, R.D.J.P., Pifarre, K.T., Ashraf, I., 2022. An effective method for lung cancer diagnosis from ct scan using deep learning-based support vector network. *Cancers* 14 (21), 5457.
- Shakeel, P.M., Burhanuddin, M.A., Desa, M.I., 2019. Lung cancer detection from CT image using improved profuse clustering and deep learning instantaneously trained neural networks. *Measurement* 145, 702–712.
- Siegel, R.L., Miller, K.D., Fuchs, H.E., Jemal, A., 2022. Cancer statistics, 2022. *CA: a Cancer J. Clin.* 72 (1).
- Sorantin, E., Grasser, M.G., Hemmelmayr, A., Tschauner, S., Hrzic, F., Weiss, V., Lacekova, J., Holzinger, A., 2021. The augmented radiologist: artificial intelligence in the practice of radiology. *Pediatr. Radiol.* 1–13.
- Suzuki, K., Kusumoto, M., Watanabe, S.I., Tsuchiya, R., Asamura, H., 2006. Radiologic classification of small adenocarcinoma of the lung: radiologic-pathologic correlation and its prognostic impact. *Ann. Thorac. Surg.* 81 (2), 413–419.
- Venkatesh, C., Ramana, K., 2022. A neural network and optimization-based lung cancer detection system in CT images. *Front. Public Health* 10, 769692.
- Wankhade, S., Vigneshwari, S., 2023. A novel hybrid deep learning method for early detection of lung cancer using neural networks. *Healthc. Anal.* 3, 100195.
- Xiuhua, G., Tao, S., Zhigang, L., 2011. Prediction models for malignant pulmonary nodules based-on texture features of CT image. In proceedings of Theory and Applications of CT Imaging and Analysis. IntechOpen.